Electron-phonon coupling and nontrivial band topology in noncentrosymmetric superconductors LaNiSi, LaPtSi, and LaPtGe

Peiran Zhang,[1] Huiqiu Yuan,[1,*] and Chao Cao[2,1,†]
[1]*Center for Correlated Matter and Department of Physics, Zhejiang University, Hangzhou, China*
[2]*Department of Physics, Hangzhou Normal University, Hangzhou, China*

(Received 27 January 2020; accepted 8 June 2020; published 18 June 2020)

The electronic structure and phonon properties of LaNiSi, LaPtSi, and LaPtGe have been studied using the first-principles density functional calculations. The electronic density of states near Fermi level of these compounds are dominated by the transition metal d orbitals and Si/Ge p orbitals, forming six sheets of Fermi surfaces. The asymmetric spin-orbit coupling lifts the spin degeneracies and creates four topological Weyl nodal rings around X points, protected by the nonsymmorphic symmetry and time-reversal symmetry. The bare-electron susceptibility does not show a prominent feature, and electron-phonon coupling is sufficient to explain the observed superconductivity.

DOI: 10.1103/PhysRevB.101.245145

I. INTRODUCTION

Inversion symmetry and time-reversal symmetry are two fundamental symmetries that profoundly affects the electronic structures and physical properties in solids, and are of particular importance for the development of superconductivity. In systems preserving inversion symmetry, the paired electrons can be classified into either spin-singlet or spin-triplet states according to their parities. The absence of inversion symmetry therefore has a significant effect on the superconducting pairing state [1–3]. In this case, the parity is no longer a good quantum number, as a result of the antisymmetric spin-orbit coupling (ASOC) effect [4–6]. Thus, the pairing state allows for the admixture of spin-singlet and spin-triplet components being conceptually different from the centrosymmetric case [7]. Noncentrosymmetric superconductivity was first observed in the heavy fermion compounds $CePt_3Si$ [8]. Later it was also found in a number of weakly correlated compounds, some of which even break time-reversal symmetry in the superconducting state [1,3,9]. In $Li_2(Pd_{1-x}Pt_x)_3B$, it was shown that the mixed pairing state might be tuned by the ASOC strength [10]. In this case, a conventional electron-phonon pairing mechanism may lead to unconventional properties, e.g., the existence of one fully opened gap and one nodal gap due to the dominant contribution from the triplet states. Since the spin degeneracy is lifted in noncentrosymmetric systems, breaking time-reversal symmetry invalidates the Kramer pair, leading to a more exotic superconducting state. For example, when magnetic field is applied in noncentrosymmetric superconductors, helical superconducting phase may present [1,11]. It was also shown that topological superconductivity may emerge in time-reversal symmetry broken noncentrosymmetric superconductors [1,12,13].

In addition to the effect in the superconducting state, these symmetries also influence the normal state in a nontrivial way. Electron states are at least doubly degenerate if both symmetries are present in a crystal. Lack of inversion center gives rise to nonzero ASOC, which lifts the SU(2) symmetry and the spin degeneracy in the normal state. This may lead to nontrivial band topologies in the normal phases [14]. In the famous tantalum monopnictide family, the ASOC gaps out most part of the nodal rings around Z and Σ, leaving only doubly degenerate nodal points, i.e., Weyl nodes [15–17]. For crystals with nonsymmorphic space groups, ASOC may also lead to other nontrivial band topologies including Weyl-type nodal rings, or hourglass semimetals [18,19].

LaTX (T = Ni, Pt; X = Si, Ge) belong to a family of noncentrosymmetric superconductors which crystallize in a body-centered tetragonal structure with nonsymmorphic symmetry (space group $I41/md$, No. 109) [20–22]. While replacing Ni with Pt in LaTX, the ASOC strength is expected to be enhanced, and the superconducting transition temperature T_c is increased from $T_c = 1.2$ K in LaNiSi to $T_c = 3.7$ K in LaPtSi [20]. Further detailed investigations of the superconducting properties of these compounds are required, although initial studies reported evidences for fully gapped s-wave behavior. By comparing with first-principles calculation results together with measurements of the specific heat, Kneidinger *et al.* proposed fully gapped s-wave superconductivity for LaPtSi [23], although the upper critical field value $H_{c2}(0)$ derived from the resistivity is significantly large than that of bulk specific heat, whose origin is still a puzzle. A previous μSR experiment on LaPtGe also suggests fully gapped superconductivity in the dirty limit [24]. More recently, however, evidence of time-reversal symmetry (TRS) breaking behavior has been observed [25]. In order to elucidate the underlying physics of these phenomena, a systematic study of the electronic structures and phonon spectra is required.

In this article we present our systematic theoretical results of the noncentrosymmetric superconductors LaTX (T = Ni,

*hqyuan@zju.edu.cn
†ccao@hznu.edu.cn

Pt; X = Si, Ge) [21–23]. Using first-principles density functional theory method, we have studied the band structure, density of states (DOS), band topology, bare electron susceptibility, and phonon properties of these compounds. The DOS of these compounds near Fermi level are dominated by the d orbitals of transition metal T and p orbitals of Si/Ge. The ASOC lifts the spin degeneracy and splits the energy band, leading to six sheets of Fermi surface. As a result, four Weyl nodal rings are buried below the Fermi level in these compounds. The bare electron susceptibility does not show any prominent feature in the whole Brillouin zone (BZ), thus the Cooper pairings are unlikely due to spin or charge fluctuations. Finally, using density functional perturbation theory, we show that the electron-phonon coupling is sufficient to explain the observed superconductivity.

The rest of this article are organized as follows. In the next section we shall briefly report the method and parameters we employed in our calculations. The electronic structure results are then presented, focusing on the band structure, DOS, and bare electron susceptibility. These results are followed by band topology analysis and phonon properties. Finally, we conclude our article.

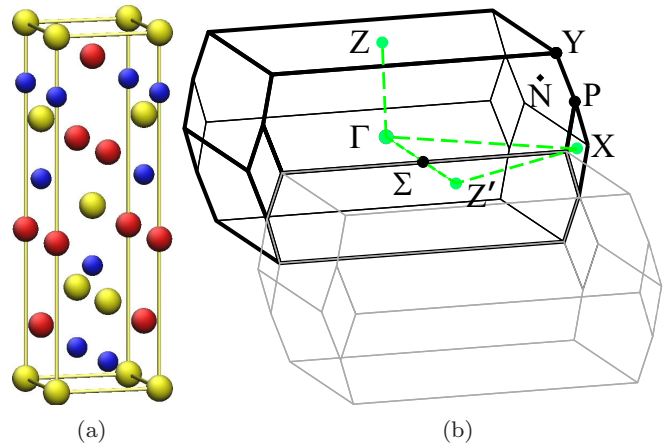

FIG. 1. (a) Conventional cell of LaTX (T = Ni, Pt; X = Si, Ge). The red, blue, and yellow atoms are La, Pt/Ni, and Si/Ge, respectively. It is worth noting that the conventional cell is twice as large as the primitive cell. (b) Brillouin zone and high symmetry points of LaTX (T = Ni, Pt; X = Si, Ge) primitive cell. The green dashed lines are the high symmetry lines used for band structure calculations. (a) Geometry; (b) BZ.

II. METHOD

The reported electronic structure of LaTX (T = Ni, Pt; X = Si, Ge) was obtained using plane-wave basis density functional method as implemented in VASP [26,27]. In particular, the projected augmented wave (PAW) method and Perdew-Burke-Ernzerhoff (PBE) flavor of generalized gradient approximation was employed. The energy cutoff was chosen to be 400 eV, and the Brillouin zone was sampled with $12 \times 12 \times 12$ K mesh to ensure the convergence. For the self-consistent calculations, we used Gaussian smearing for Brillouin zone integration, while the tetrahedra method was employed to calculate the DOS. Both the lattice constants and the atomic internal coordinates were optimized so that forces on each atom were smaller than 0.01 eV/Å and internal stress less than 0.1 kbar. The first-principles results were then fitted to a tight-binding model Hamiltonian using maximally localized Wannier functions (MLWF) [28,29] for both calculations with and without SOC. The results were then used to determine the topological properties of the band structure. For phonon related properties, we have employed density functional perturbation theory as implemented in QUANTUM ESPRESSO (QE) [30]. The geometry and electronic structure obtained by QE were also carefully checked against the results from VASP.

III. RESULTS AND DISCUSSION

The LaTX (T = Ni, Pt; X = Si, Ge) compounds crystallize in noncentrosymmetric body-centered tetragonal phase with nonsymmorphic symmetry (space group $I4_1/md$, No. 109). The crystal structure and its Brillouin zone are shown in Fig. 1. This space group contains two mirror planes (M_x and M_y), as well as two gliding mirror planes (M_{xy} and $M_{\bar{x}y}$). The relaxed lattice constants and internal coordinates of each compound are summarized in Table I.

A. Electronic structure

The calculated band structures of LaTX (T = Ni, Pt; X = Si, Ge) are shown in Fig. 2, which shows rather similar behavior. Thereafter, we will elucidate the band dispersion based on the results of LaPtGe, unless it is specified otherwise. For LaPtGe, the La-5d, Pt-5d, and Ge-4p orbitals dominate the electronic states of the conduction band from $E_F - 5.5$ eV to $E_F + 1.5$ eV. Without spin-orbit coupling (SOC), three bands (six bands including spin degeneracy) crosses the Fermi level, forming three Fermi surface sheets. Two of these bands located at approximately $E_F - 0.4$ eV and $E_F + 0.5$ eV are nearly flat from Γ to Z, while the one formed by Pt-5d_{z^2} and La-5$d_{x^2-y^2}$ is very dispersive and crosses the Fermi level. The LaPtSi band structure is similar, whereas the LaNiSi bands are less dispersive than both LaPtGe and LaPtSi, indicated by its reduced bandwidth (from $E_F - 4.5$ eV to $E_F + 1.5$ eV), and is most prominent on the bands crossing the Fermi level between Z' and X [Figs. 2(a) and 2(c)]. Close to the Fermi level, both Pt-5d and Ni-3d orbitals have significant contribution to the DOS, therefore substitution of Pt by Ni is expected to strongly affect the SOC splitting. The contribution from Si-3p or Ge-4p orbitals are mainly located ∼0.4 eV below Fermi

TABLE I. Lattice constants and internal coordinates of each compound. The lattice constants are in Angstroms, whereas the coordinates of the atoms are in units of the lattice constants.

	LaNiSi	LaPtSi	LaPtGe
a	4.1860	4.2734	4.2954
c	14.0123	14.6244	15.1543
La	0.000, 0.000, 0.579	0.000, 0.000, 0.580	0.000, 0.000, 0.580
T	0.000, 0.000, 0.168	0.000, 0.000, 0.167	0.000, 0.000, 0.165
X	0.000, 0.000, 0.000	0.000, 0.000, 0.000	0.000, 0.000, 0.000

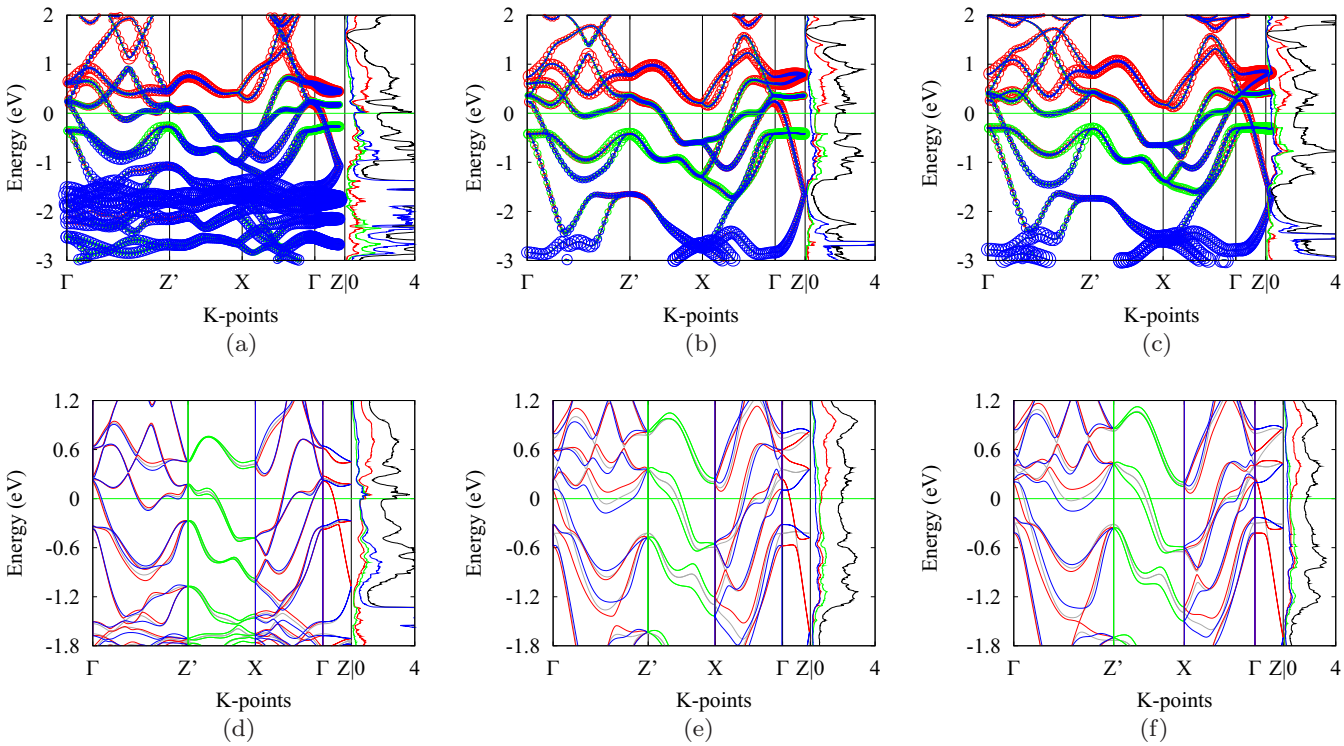

FIG. 2. Band structure and DOS of LaNiSi (a) and (d), LaPtSi (b) and (e), and LaPtGe (c) and (f) without (a)–(c) and with SOC (d)–(f). In the left panels of (a)–(c), the sizes of red, blue, and green circles are proportional to La-5d, Pt-5d/Ni-3d, and Si-3p/Ge-4p orbital weights; while in the right panels, the black, red, blue, and green lines represent total DOS, projected DOS of La-5d, Pt-5d/Ni-3d, and Si-3p/Ge-4p orbitals, respectively. In (d)–(f), the gray lines are results without SOC for comparing purposes. The red (blue) lines are states with i ($-i$) eigenvalues for M_x along Γ-Z', $-i$ (i) eigenvalues for gliding mirror along Γ-X, as well as states with $e^{\pm i\pi/4}$ ($e^{\pm 3i\pi/4}$) eigenvalues for screw symmetry along Γ-Z.

level. As a result, the substitution of Si by Ge only moderately affects SOC splitting.

Figures 2(d)–2(f) shows the band structures of LaTX (T = Ni, Pt; X = Si, Ge) with SOC. Since the crystal structure lacks an inversion center, the spin degeneracy is lifted at general k points once SOC is considered, therefore the Fermi surfaces of these materials consist of six sheets. The states remain doubly degenerate along X-Z' as well as Γ-Z due to the gliding mirror or screw symmetries. In particular, the crystal symmetry and time-reversal symmetry allows only fourfold degenerate state at Z point. By fitting the DFT results to a tight-binding Hamiltonian using the maximally localized Wannier functions (MLWF) method [28], we constructed the Fermi surfaces of these materials. Among the six Fermi surface sheets, two of them are 3D drumlike enclosing the Γ point, two are quasi-2D cylindrical around X point, and two are extended open 3D sheets [Fig. 3(a)]. Once SOC is considered, the shape of the 3D drumlike sheets around Γ and the two quasi-2D cylindrical sheets around X are similar, although their volumes vary due to the ASOC splitting [Fig. 3(b)]. One of the extended open 3D sheets becomes even more extended, forming an open Fermi surface at $k_z = \pi$ plane. Therefore the electronic structure of these compounds are mainly three dimensional despite its large c/a ratio. The DOS at the Fermi level are $n(E_F) = 1.78$, 2.01, and 2.87 states/(eV^{-1} f.u.), corresponding to $\gamma_e = 4.19$, 4.74, and 6.76 mJ/(mol K^2) for LaPtGe, LaPtSi, and LaNiSi, respectively. Experimentally, the specific heat measurement yields $\gamma = 6.6$ [24], 6.5 [23], and 8.89 mJ/(mol K^2) [21] for LaPtSi and LaNiSi, respectively. Assuming $\gamma = \gamma_e(1 + \gamma_{\text{elph}})$, we obtain γ_{elph} ranging from 0.3 to 0.6 for the LaTX (T = Ni, Pt; X = Si, Ge) family. These values are comparable to previous calculation results [23].

Using the same tight-binding Hamiltonian, we have also calculated the static bare electron susceptibility $\chi_0(\mathbf{q})$ using

$$\chi_0(\mathbf{q}) = \frac{1}{N_\mathbf{k}} \sum_{mn} \sum_{\mu\nu\mathbf{k}} \frac{\langle m|\mu\mathbf{k}\rangle\langle\mu\mathbf{k}|n\rangle\langle n|\nu\mathbf{k}+\mathbf{q}\rangle\langle\nu\mathbf{k}+\mathbf{q}|m\rangle}{\epsilon_{\nu\mathbf{k}+\mathbf{q}} - \epsilon_{\mu\mathbf{k}} + i0^+} \times (f_{\mu\mathbf{k}} - f_{\nu\mathbf{k}+\mathbf{q}}),$$

where $\epsilon_{\mu\mathbf{k}}$ and $f_{\mu\mathbf{k}}$ are the band energy (measured from E_F) and occupation number of Bloch state $|\mu\mathbf{k}\rangle$, respectively; $|n\rangle$ denotes the nth Wannier orbital; and $N_\mathbf{k}$ is the number of the $\mathbf{k}$ points used for the irreducible Brillouin zone (IBZ) integration. The imaginary part of χ_0 is obtained by calculating the nesting function [31] using

$$f(\mathbf{q}) = \frac{1}{N_\mathbf{k}} \sum_{\mathbf{k}} \delta(\epsilon_{\mu\mathbf{k}})\delta(\epsilon_{\nu\mathbf{k}+\mathbf{q}}).$$

The resulting real part of χ_0 of LaNiSi, LaPtSi, or LaPtGe are almost completely flat within the whole BZ [Fig. 3(c)]. This is consistent with the fact that these materials are nonmagnetic. The imaginary part of χ_0 has a small hump close to the middle of Γ-Z', but this feature is absent in either LaPtSi or LaPtGe [32]. Therefore the charge or spin fluctuation is expected to

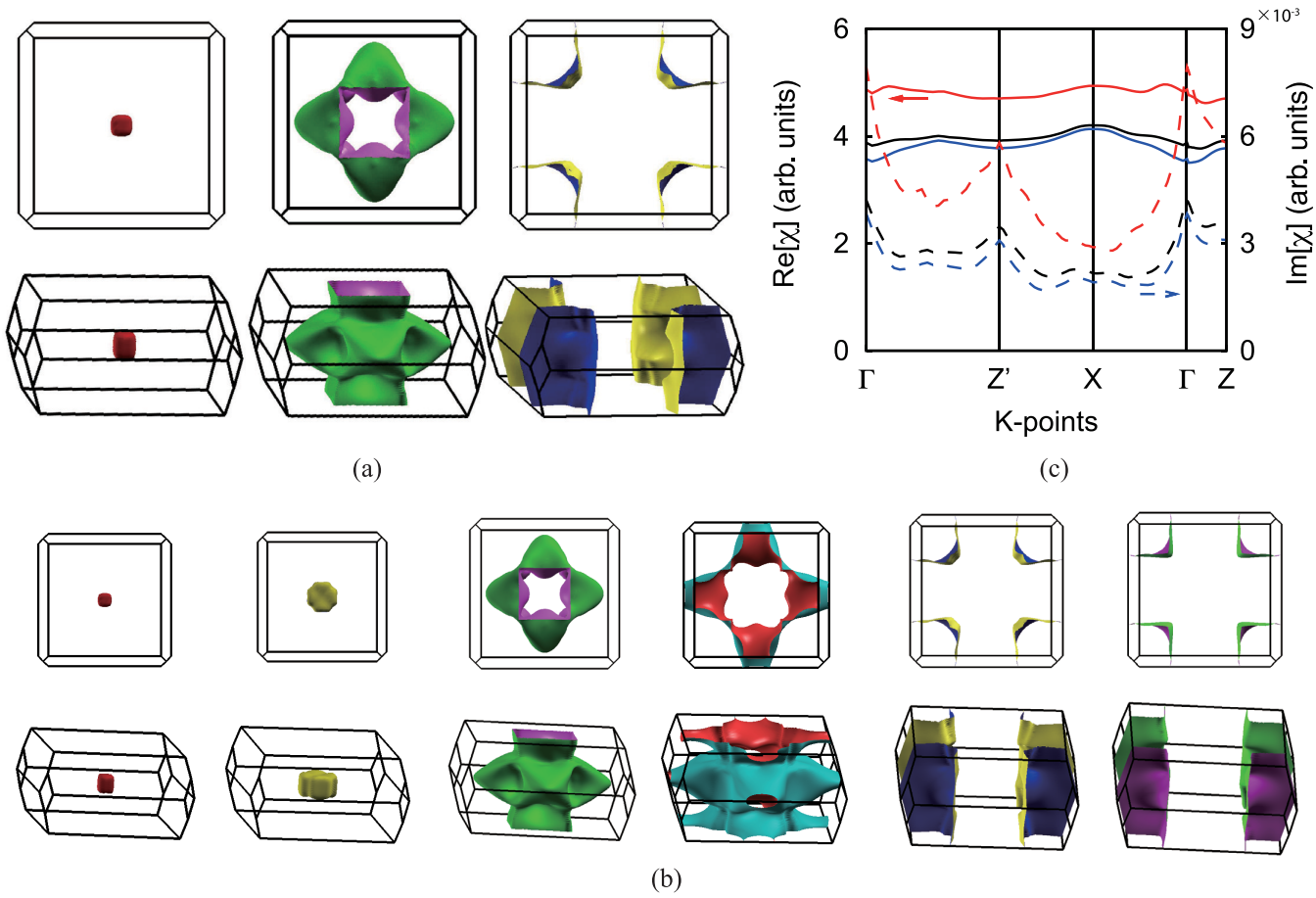

FIG. 3. (a) Fermi surface of LaPtGe without SOC, (b) Fermi surface of LaPtGe with SOC, and (c) bare electron susceptibility χ_0 of LaTX (T = Ni, Pt; X = Si, Ge). (c) The red/black/blue lines are for LaNiSi/LaPtSi/LaPtGe, whereas the solid (dashed) lines are the real (imaginary) parts of χ_0, respectively.

be negligible in these material, and the pairing mechanism are most likely to be conventional BCS electron-phonon coupling.

B. Topological properties

We first identify some common features of the band structure in these compounds. Without SOC, there are three pairs of doubly degenerate bands crossing the Fermi level, we label them from low energy to high energy as bands 1/2, 3/4, and 5/6. Noticing that the electron count fills to band 4, therefore we shall study the band crossings between bands 4 and 5. Under SOC, the spin degeneracy at general k points are lifted due to lack of the inversion symmetry. However, the Kramer pairs are preserved due to the preserved time-reversal symmetry at all time-reversal invariant momenta (TRIM), including Γ (0, 0, 0), N (0, π, 0), X (0, 0, π), and Z (π, π, π) in these materials. Therefore, only doubly degenerate Γ_5 states can exist at Z. Each pair of Γ_5 states share the same eigenvalues of gliding mirror operation $\{M_{xy}|(1/4, 3/4, 1/2)\}$, which can be either $+i$ or $-i$, yielding Γ_5^+ or Γ_5^- states. We note that bands 3/4 and 5/6 are Γ_5^- and Γ_5^+ states, respectively. In addition, all states along Γ-X can be classified using the eigenvalues of this gliding mirror operation, as we can see from Fig. 4(a) as well as Figs. 2(d)–2(f). At Γ point, all states are also doubly degenerate due to Kramer pairs, therefore only doubly degenerate Γ_6 and Γ_7 states can exist. These states, however, contain a pair of states yielding opposite eigenvalues of gliding mirror operation $\{M_{xy}|(1/4, 3/4, 1/2)\}$. Combining the above requirements, one can immediately see that band crossings are guaranteed between Γ and X if the number of valence electrons $\nu \neq 4n$. In fact, $\nu = 30$ for all the compounds we investigated. Therefore, there must be a band crossing due to band 4/5 between Γ and X. Since all states on the Γ-Z-X plane can be classified using $\{M_{xy}|(1/4, 3/4, 1/2)\}$, there must be a nodal ring surrounding X point on this plane.

Using the tight-binding Wannier orbital based Hamiltonian, we have searched for nodal points formed by bands 4 and 5 in the whole BZ in all these compounds. All three compounds we investigated have produced four nodal rings around X points, confirming the above analysis [Fig. 4(c)]. Nevertheless, the nodal rings are most observable (largest) in LaPtGe, where the SOC is strongest. Using the Wilson loop method, we calculated the Berry phase around these rings, and the results are π, meaning these nodal rings are topologically nontrivial. Since all the states on the nodal ring are doubly degenerate, we conclude that these nodal rings must be Weyl type. Again, we would like to stress that the existence of the nodal rings around X is completely due to time-reversal symmetry, the gliding mirror symmetry, the screw symmetry, and the electron filling. Apart from these

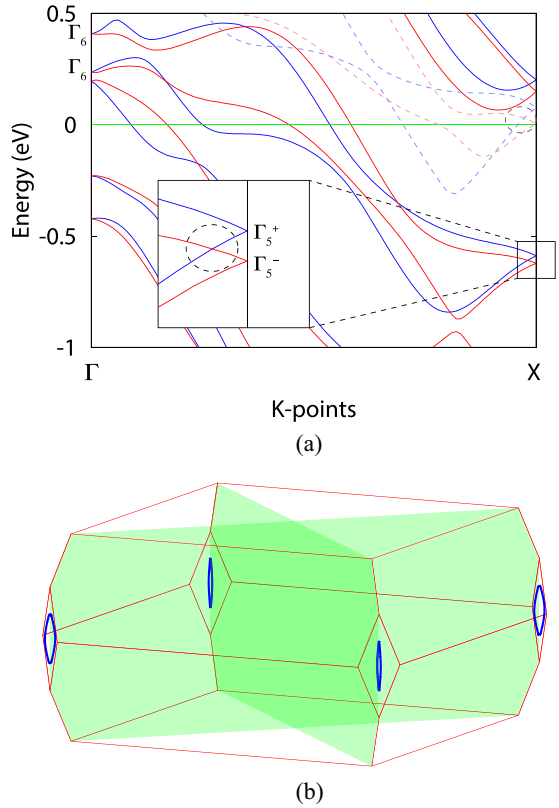

FIG. 4. (a) LaPtGe SOC band structure from Γ-X. The dashed lines in light-blue/light-red are the same $\Gamma_5^{\pm}$ states in LaIrGe. Notice the band-crossing feature is above the Fermi level in LaIrGe. (b) Nodal rings in LaPtGe. The blue (red) lines indicate eigenvalue i $(-i)$ of gliding mirror operation $\{M_{xy}|(1/4, 3/4, 1/2)\}$. The existence of the nodal structure [as indicated by the dashed circle in the inset of (a)] is guaranteed by band symmetries at Γ and X.

symmetry-protected topological nodal rings, there are also numerous isolated doubly degenerate points. However, there is no symmetry argument associated with these points. It is worthy noting that while the nodal rings are ∼0.5 eV below the Fermi levels, the band states forming these rings are still partially occupied. Therefore, these states can still contribute to transport properties including topological Hall effect, which results from all occupied states [33–35]. In addition, we notice that these nodal rings can be tuned close to the Fermi level by hole doping. In fact, we have also performed calculations for isostructural LaIrGe. These nodal rings are also present in LaIrGe, and they appear above the Fermi level [dashed lines in Fig. 4(a)].

C. Phonon dispersion and electron-phonon coupling

To identify the underlying pairing mechanism of superconductivity, we have also performed phonon and electron-phonon calculations using DFPT (Fig. 5). The phonon spectrum do not exhibit instability in these lattices. In general, the 18 phonon modes can be divided into 3 parts: part 1 are the lowest 12 modes ranging from 0 to a characteristic frequency ω_0, part 3 are the highest 4 modes above 8 THz, and part 2 are the 2 modes in between. From projected phonon DOS, we identify the modes in parts 2 and 3 are mostly due to Si/Ge atoms, and the modes in part 1 are due to La and Ni/Pt atoms. For LaNiSi, ω_0 is approximately 6 THz, and the electron-phonon coupling is strongest at Z on the lowest phonon frequency [Fig. 5(a)]. This is the scissoring mode where the La atoms and Ni/Si atoms move in opposite direction [left panel of Fig. 5(c)]. For LaPtSi, since Pt atoms are much heavier than Ni, the phonon mode frequencies in region 1 are strongly reduced, and ω_0 is suppressed by approximately 1/3. Thus, the Debye frequency and $\omega_{\log}$ frequency are expected to be much reduced in LaPtSi. In fact, $\omega_{\log} = 169.5$ and 140.6 K in LaNiSi and LaPtSi, respectively. The largest electron-phonon coupling is contributed by a soft phonon mode at the middle of the Γ-Z' line $(1/4, -1/4, -1/4)$. This mode is a scissoring mode within one of the Pt layers. Previous calculations have also reported this soft mode [23], which was attributed to the Fermi surface nesting. However, this argument is not supported in our bare-electron susceptibility calculations [Fig. 3(b)], since the nesting function is flat in LaPtSi or LaPtGe. Instead, our electron-phonon coupling calculation provides unambiguous evidence that the phonon softening is due to large enhancement of electron-phonon coupling at this **q** point. In extreme cases of such enhancement, the soft phonon could eventually

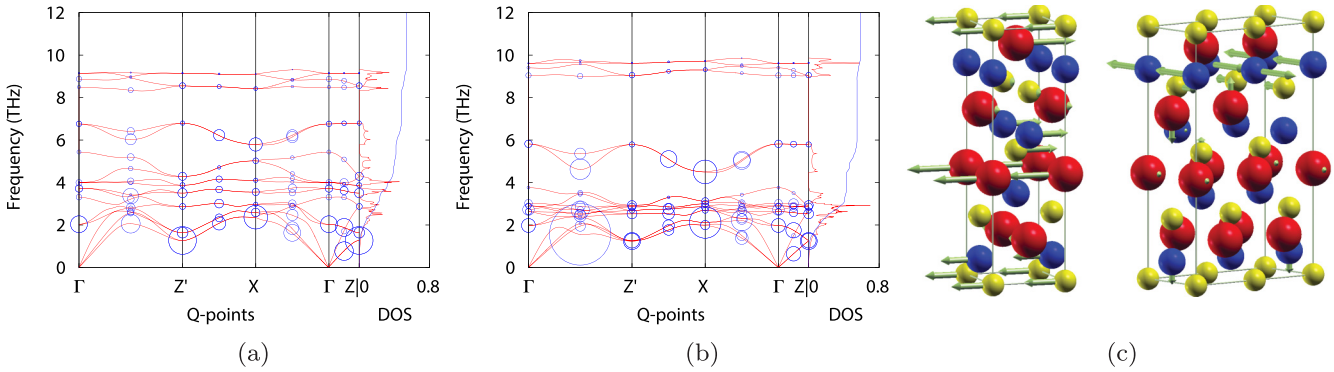

FIG. 5. (a) and (b) Phonon spectrum and DOS for (a) LaNiSi and (b) LaPtSi. The size of the blue circles are proportional to the electron-phonon coupling strength of the specific phonon mode. In the DOS panels, the red lines are the phonon DOS, while the blue lines are the integrated Eliashberg function $\lambda(\omega) = 2\int_0^{\omega} \alpha^2 F(\omega')/\omega' d\omega'$. (c) The phonon modes yielding largest electron-phonon coupling. Left panel is the lowest energy mode at Z in LaNiSi, right panel is the lowest energy mode (soft mode) in between Γ and Z'.

lead to a charge-density wave (CDW) transition [36]. The total electron-phonon coupling constant is obtained by integrating the Eliashberg function $\lambda = 2\int_0^\infty \alpha^2F(\omega)/\omega d\omega$, and are approximately 0.49 and 0.59, respectively, for LaNiSi and LaPtSi. These values are in line with the estimated electron-phonon coupling constants γ_{elph} from DOS and specific heat measurement results. These in turn yields superconducting $T_c = 1.94$ and 3.06 K for LaNiSi and LaPtSi from the Allen-Dynes equation $T_c = \frac{\omega_{\log}}{1.2}\exp\left(-\frac{1.04(1+\lambda)}{\lambda-\mu^*(1+0.62\lambda)}\right)$ (μ^* is chosen to be 0.1 in both calculations). These values are in good agreement with experimental observations. Therefore, we conclude that the superconductivity in this family is due to electron-phonon coupling BCS mechanism. This is in agreement with previous experimental results [23,24].

IV. DISCUSSION AND CONCLUSION

In conclusion, we have performed systematic first-principles study of LaNiSi, LaPtSi, and LaPtGe. All these compounds are noncentrosymmetric superconductors with $I4_1/md$ space group. Due to the nonsymmorphic symmetry operations and time-reversal symmetry, topologically protected nodal rings exist on the gliding mirror planes of these materials around X points. These nodal rings can be tuned close to the Fermi level with appropriate Ir doping. The bare-electron susceptibility do not show prominent features, suggesting minimum spin or charge fluctuations. The soft phonon mode at $(1/4, -1/4, -1/4)$ in LaPtSi is mainly due to enhancement of momentum resolved electron-phonon coupling. The superconductivity in these materials can be well explained with electron-phonon BCS mechanism. Combining the nontrivial band topology and fully gapped superconductivity, these materials may be candidate to possible topological superconductivity.

ACKNOWLEDGMENTS

This work has been supported by the NSFC (Grants No. 11874137, No. 11974306, and No. U1632275) and National Key R&D Program of China (Grants No. 2016YFA0300202 and No. 2017YFA0303100). All the calculations were done on the High Performance Computing Center of CCM at Zhejiang University.

[1] M. Smidman, M. B. Salamon, H. Q. Yuan, and D. F. Agterberg, Rep. Prog. Phys. **80**, 036501 (2017).
[2] E. Bauer and M. Sigrist (Eds.), *Non-Centrosymmetric Superconductors: Introduction and Overview*, Lecture Notes in Physics, Vol. 847 (Springer, Berlin, 2012).
[3] W. Xie, P. Zhang, B. Shen, W. Jiang, G. Pang, T. Shang, C. Cao, M. Smidman, and H. Yuan, Sci. China: Phys., Mech. Astron. **63**, 237412 (2020).
[4] G. Dresselhaus, Phys. Rev. **100**, 580 (1955).
[5] L. M. Roth, Phys. Rev. **173**, 755 (1968).
[6] E. I. Rashba, Sov. Phys. Solid State **2**, 1109 (1960).
[7] P. A. Frigeri, D. F. Agterberg, A. Koga, and M. Sigrist, Phys. Rev. Lett. **92**, 097001 (2004).
[8] E. Bauer, G. Hilscher, H. Michor, C. Paul, E. W. Scheidt, A. Gribanov, Y. Seropegin, H. Noël, M. Sigrist, and P. Rogl, Phys. Rev. Lett. **92**, 027003 (2004).
[9] T. Shang, M. Smidman, A. Wang, L.-J. Chang, C. Baines, M. K. Lee, Z. Y. Nie, G. M. Pang, W. Xie, W. B. Jiang, M. Shi, M. Medarde, T. Shiroka, and H. Q. Yuan, Phys. Rev. Lett. **124**, 207001 (2020).
[10] H. Q. Yuan, D. F. Agterberg, N. Hayashi, P. Badica, D. Vandervelde, K. Togano, M. Sigrist, and M. B. Salamon, Phys. Rev. Lett. **97**, 017006 (2006).
[11] M. Sigrist, D. Agterberg, P. Frigeri, N. Hayashi, R. Kaur, A. Koga, I. Milat, K. Wakabayashi, and Y. Yanase, J. Magn. Magn. Mater. **310**, 536 (2007), proceedings of the 17th International Conference on Magnetism.
[12] P. Ghosh, J. D. Sau, S. Tewari, and S. Das Sarma, Phys. Rev. B **82**, 184525 (2010).
[13] A. P. Schnyder and S. Ryu, Phys. Rev. B **84**, 060504(R) (2011).
[14] M. N. Ali, Q. D. Gibson, T. Klimczuk, and R. J. Cava, Phys. Rev. B **89**, 020505(R) (2014).
[15] S.-Y. Xu, I. Belopolski, D. S. Sanchez, C. Zhang, G. Chang, C. Guo, G. Bian, Z. Yuan, H. Lu, T.-R. Chang, P. P. Shibayev, M. L. Prokopovych, N. Alidoust, H. Zheng, C.-C. Lee, S.-M. Huang, R. Sankar, F. Chou, C.-H. Hsu, H.-T. Jeng, A. Bansil, T. Neupert, V. N. Strocov, H. Lin, S. Jia, and M. Z. Hasan, Sci. Adv. **1**, e1501092 (2015).
[16] H. Weng, C. Fang, Z. Fang, B. A. Bernevig, and X. Dai, Phys. Rev. X **5**, 011029 (2015).
[17] Y. Sun, S.-C. Wu, and B. Yan, Phys. Rev. B **92**, 115428 (2015).
[18] S.-Y. Xu, N. Alidoust, I. Belopolski, Z. Yuan, G. Bian, T.-R. Chang, H. Zheng, V. N. Strocov, D. S. Sanchez, G. Chang, C. Zhang, D. Mou, Y. Wu, L. Huang, C.-C. Lee, S.-M. Huang, B. Wang, A. Bansil, H.-T. Jeng, T. Neupert, A. Kaminski, H. Lin, S. Jia, and M. Zahid Hasan, Nat. Phys. **11**, 748 (2015).
[19] L. Wang, S.-K. Jian, and H. Yao, Phys. Rev. B **96**, 075110 (2017).
[20] W. Lee, Solid State Commun. **94**, 425 (1995).
[21] W. H. Lee, F. A. Yang, C. R. Shih, and H. D. Yang, Phys. Rev. B **50**, 6523 (1994).
[22] J. Evers, G. Oehlinger, A. Weiss, and C. Probst, Solid State Commun. **50**, 61 (1984).
[23] F. Kneidinger, H. Michor, A. Sidorenko, E. Bauer, I. Zeiringer, P. Rogl, C. Blaas-Schenner, D. Reith, and R. Podloucky, Phys. Rev. B **88**, 104508 (2013).
[24] Sajilesh K. P., D. Singh, P. K. Biswas, A. D. Hillier, and R. P. Singh, Phys. Rev. B **98**, 214505 (2018).
[25] T. Shang, H. Yuan *et al.* (unpublished).
[26] G. Kresse and J. Hafner, Phys. Rev. B **47**, 558 (1993).
[27] G. Kresse and D. Joubert, Phys. Rev. B **59**, 1758 (1999).
[28] I. Souza, N. Marzari, and D. Vanderbilt, Phys. Rev. B **65**, 035109 (2001).
[29] A. A. Mostofi, J. R. Yates, Y.-S. Lee, I. Souza, D. Vanderbilt, and N. Marzari, Comput. Phys. Commun. **178**, 685 (2008).
[30] P. Giannozzi, S. Baroni, N. Bonini *et al.*, J. Phys.: Condens. Matter **21**, 395502 (2009).

[31] We employed 160 Wannier orbitals and k mesh of $48 \times 48 \times 48$ to calculate χ_0. Electronic temperature is chosen to be 10 meV when calculating the occupation function f and δ function.

[32] The peak at Γ is spurious because the width of this peak strongly depends on the electronic temperature T_{el}, which goes to 0 as $T_{\mathrm{el}} \to 0$.

[33] E. Liu, Y. Sun, N. Kumar, L. Muechler, A. Sun, L. Jiao, S.-Y. Yang, D. Liu, A. Liang, Q. Xu, J. Kroder, V. Süß, H. Borrmann, C. Shekhar, Z. Wang, C. Xi, W. Wang, W. Schnelle, S. Wirth, Y. Chen, S. T. B. Goennenwein, and C. Felser, Nat. Phys. **14**, 1125 (2018).

[34] Q. Wang, Y. Xu, R. Lou, Z. Liu, M. Li, Y. Huang, D. Shen, H. Weng, S. Wang, and H. Lei, Nat. Commun. **9**, 3681 (2018).

[35] H. Yang, W. You, J. Wang, J. Huang, C. Xi, X. Xu, C. Cao, M. Tian, Z.-A. Xu, J. Dai, and Y. Li, Phys. Rev. Mater. **4**, 024202 (2020).

[36] M. D. Johannes and I. I. Mazin, Phys. Rev. B **77**, 165135 (2008).